Dendritic synaptic integration modes under *in vivo*-like states

Cesar C. Ceballos[1], Rodrigo F. O. Pena[1,2 *]

[1] Department of Biological Sciences, Florida Atlantic University, Jupiter, FL 33458, USA

[2] Stiles-Nicholson Brain Institute, Florida Atlantic University, Jupiter, FL 33458, USA

* Corresponding author

E- mail: penar@fau.edu

Abstract

The neural code remains undiscovered and understanding synaptic input integration under *in vivo*-like conditions is just the initial step toward unraveling it. Synaptic signals generate fast dendritic spikes through two main modes of temporal summation: coincidence detection and integration. In coincidence detection, dendrites fire only when multiple incoming signals arrive in rapid succession, whereas integration involves summation of postsynaptic potentials over longer periods with minimal membrane leakage. This process is influenced by ionic properties, especially as the membrane potential approaches the firing threshold, where inactivating currents play a critical role. However, the modulation of temporal summation by these currents under *in vivo*-like conditions has not been thoroughly studied. In our research, we used computer simulations of a single dendritic branch to investigate how three inactivating currents — A-type potassium, T-type calcium, and transient sodium — affect temporal summation. We found that calcium and sodium currents promote integrative behavior in dendrites, while potassium currents enhance their ability to act as coincidence detectors. By adjusting the levels of these currents in dendrites, neurons can flexibly switch between integration and coincidence detection modes, providing them with a versatile mechanism for complex tasks like multiplexing. This flexibility could be key to understanding how neural circuits process information in real time.

Significance

Neurons consist of specialized structures that shape computation. The soma processes inputs from dendrites and communicates via its axon. Dendrites have a branched architecture. They receive excitatory signals and generate dendritic spikes. These spikes allow individual branches to convert inputs into spiking patterns prior to somatic integration. Depending on input synchrony, branches operate as coincidence detectors or integrators, which is determined by ionic currents. Our study explores how these currents affect signal summation. We found that potassium currents favor coincidence detection, while calcium and sodium currents promote integration. Cellular mechanisms finely tune these currents, enabling dendrites to adjust processing modes in response to synaptic inputs.

Introduction

It is well known that dendrites can fire sodium, calcium and NMDA dependent action potentials (dendritic spikes) under *in vivo* conditions at higher frequency than found at the soma (Moore et al. 2017). These suggests the existence of dendritic synaptic integration and transformation into dendritic spikes as a first stage of neuronal processing (Ujfalussy et al. 2018). Understanding the neural code involves learning how dendrites process synaptic inputs and transform them into dendritic spikes via temporal summation (Stuart et al. 2015; Dembrow et al. 2022). Two key summation types, coincidence detection and integration, are critical for neural coding (Brette 2015; Ratté et al. 2013; Hong et al. 2012; Stoll et al. 2023). Coincidence detection occurs when a dendrite fires a spike after receiving multiple signals within a short interval, while integration mode allows voltage accumulation over time until a spike fires (Dembrow et al. 2015; Dembrow et al. 2022; Roome et al. 2020). Dendrites exhibit both modes, with Purkinje neurons dendrites functioning as coincidence detectors and L5 dendrites in medial prefrontal cortex acting as

integrators (Dembrow et al. 2015; Roome et al. 2020). These modes influence the transmission of information via firing rates or synchronized spikes (Hong et al. 2012).

These synaptic summation modes form a continuum from coincidence detection to perfect integration (Rudolph et al. 2003; Prince et al. 2021). The specific mode of summation depends on the composition of ionic currents in the dendritic membrane, which modulate synaptic temporal properties (Azouz et al. 2000; Prince et al. 2021). Strong potassium currents are linked to coincidence detection, while sodium and calcium currents support perfect integration (Mathews et al. 2010; Farries et al. 2010; Branco et al. 2016; Prescott and De Koninck 2005). Adjusting the expression of these currents allows a range of temporal summation modes.

Dendritic inactivating currents are crucial for near-threshold synaptic summation, as shown by studies on A-type potassium currents influencing theta oscillations and temporal summation (Bourdeau et al. 2007; Rathour et al. 2016). Excitatory postsynaptic potentials (EPSPs) are amplified by T-type calcium currents, enhancing temporal precision (Fukaya et al. 2018), while transient sodium currents act at subthreshold potentials (Carter et al. 2012; Stuart et al. 2015). Further research is needed to explore inactivation's role in dendritic properties.

A complete understanding requires examining currents with (i) established, (ii) less established, and (iii) inconsistent effects. (i) Non-inactivating currents like M-type potassium reduce EPSP amplitude and shorten decay (Hönigsperger et al. 2015; Peng et al. 2017; Liu et al. 2008), while persistent sodium currents amplify and prolong EPSPs (Ceballos et al. 2017b; Liu et al. 2008; Hsu et al. 2018). (ii) Inactivating currents, such as A-type potassium, consistently reduce EPSP

amplitude (Hoffman et al. 1997; Mathews et al. 2010; Bourdeau et al. 2007; Rathour et al. 2016). (iii) Calcium currents show mixed effects: some studies report no impact on amplitude or decay (Stuart et al. 1995; González-Burgos et al. 2001; Andreasen et al. 1999; Hsu et al. 2018; Seong et al. 2014), others show effects on amplitude (Fukaya et al. 2018; Gillessen et al. 1997), only on decay (Prescott et al. 2005), or both (Liu et al. 2008; Connelly et al. 2016; Urban et al. 1998; Evans et al. 2017; Deleuze et al. 2012). Transient sodium currents also show variable effects: some studies report no effect (Connelly et al. 2016; Grunditz et al. 2008), while others show amplification of EPSPs (Carter et al. 2012; Hage et al. 2016) or Tetrodotoxin-sensitive prolonged decay (Ceballos et al. 2018). Sodium-dependent EPSP amplification has been observed *in vivo* (Hsu et al. 2018).

Most EPSP studies are not easily transferable to *in vivo* situations, where neural coding is better understood. *In vivo*, large depolarization states occur during neuronal oscillations like theta oscillations (Adam et al. 2019; Malezieux et al. 2020). These states bring the membrane potential near the threshold, suggesting the activation of inactivating currents (Hsu et al. 2018), though little is known about how these conductances affect synaptic summation *in vivo*. This raises questions about how these currents filter synaptic signals and determine synaptic summation modes.

Experimental results and computational modeling suggest that neurons process synaptic inputs via a two-stage integration process. In this process, synaptic inputs are integrated in individual dendritic branches, generating dendritic spikes that propagate to the axon, where global summation occurs (Katz, 2009; Polsky, 2004). Based on these findings, we developed a computational model

of a single dendritic branch in which *in vivo*-like synaptic input activates voltage-dependent currents, and the corresponding synaptic potentials are integrated to generate dendritic spikes.

Understanding how ionic currents shape membrane temporal properties is essential for dendritic computation, influencing whether dendrites function as integrators or coincidence detectors. This paper explores the effects of A-type potassium, T-type calcium, and transient sodium currents on synaptic temporal summation *in vivo*-like conditions, focusing on their impact on voltage traces and summation properties (integrator vs. coincidence detector).

Methods

Below, we introduce the single dendritic branch model, describe its embedded ionic currents, explain how the simulations were performed, and detail the mathematical analysis used to understand how these currents reduce/contract and amplify/prolong signals.

Single dendritic branch model

We built a point-neuron model of a single dendritic branch with ionic currents, using the Hodgkin–Huxley formalism. The most general case of a Hodgkin-Huxley (HH) current involves two gating variables: p for activation and q for inactivation. This type of current is referred to as "inactivating" and acts as a break to close the channel (Hille, 2001). Each gating process has its own time constant, denoted as τ_{act} for activation and τ_{inact} for inactivation.

The current equation is

$$C\frac{dv}{dt} = \sum_{i=1}^{n} I_i(v) + I_{inj}, \qquad \text{(Eq 1)}$$

where C is the capacitance, v is the voltage, $I_i(v)$ is the voltage-dependent current, n is the number of ionic currents and I_{inj} is the injected current. In our paper, ionic currents will be represented using the HH formalism:

$$I_i = \bar{g}_i p_i q_i \left(V - E_{rev}^i\right), \qquad \text{(Eq 2)}$$

where $\bar{g}_i$ is the maximum conductance, E_{rev}^i the reversal potential, and for (x=p,q) we have

$$\frac{dx}{dt} = \frac{x^\infty - x}{\tau_{act/inact}}. \qquad \text{(Eq 3)}$$

In Eq. 3, x^∞ is the steady-state activation variable and it is represented by a sigmoid function following

$$x^\infty(v) = \frac{1}{1+e^{\left(\frac{V-V_{1/2}}{-k}\right)}}. \qquad \text{(Eq 4)}$$

Where $V_{1/2}$ and k are constants. Importantly, $p = p(v,t)$ and $q = q(v,t)$, i.e., activation and inactivation variables are dependent on voltage and time.

In this paper we only address inactivating currents activated by depolarization such as transient sodium, A-type potassium and T-type calcium. One important mathematical property of p and q in this situation that can be derived from the fact that they are activation and inactivation

137 functions is that $\frac{\partial p}{\partial v} > 0$ and $\frac{\partial q}{\partial v} < 0$, although p > 0 and q > 0. This behavior occurs for currents

138 activated by depolarization, opposed to when the currents are activated by hyperpolarization

139 ($\frac{\partial p}{\partial v} < 0$ and $\frac{\partial q}{\partial v} > 0$).

140

141 Importantly, many inactivating potassium, sodium, and calcium currents follow Equation 2,

142 while some variations of this equation exist where the activation or inactivation variables are

143 raised to an exponent (such as 2, 3 or 4). Thus, the equation can be represented as $I_i =$

144 $\bar{g}_i {p_i}^x {q_i}^y (V - E_{rev}^i)$. Although we will use this representation in our simulations, we will use the

145 simple version as shown in Eq.2 for the analytical approximation.

146

147 We performed computer simulations using custom-made codes in Matlab. Three types of

148 currents were investigated: A-type potassium, T-type calcium and transient sodium. Capacitance

149 density was 1μF/cm^2. Activation variables were defined by the following parameters: for

150 potassium: $V_{1/2}$ = -50 mV, k = 15, for calcium: $V_{1/2}$ = -50 mV, k = 15, and for sodium: $V_{1/2}$ = -30

151 mV, k = 5. Inactivation variables were defined by the following parameters: for potassium: $V_{1/2}$ =

152 -60, k = 15, for calcium: $V_{1/2}$ = -60 mV, k = 15, and for sodium: $V_{1/2}$ = -60 mV, k = 5. Activation

153 kinetics was τ_{act} = 0.2, 0.5 and 0.05 ms for potassium, calcium and sodium respectively.

154 Inactivation kinetics was τ_{inact} = 5, 10 and 0.5 ms for potassium, calcium and sodium

155 respectively. Conductance densities were expressed as mS/cm^2 with values: g_K = 1, g_{Ca} = 0.1 and

156 g_{Na} = 50. Leak conductance density was 0.3 mS/cm^2. Reversal potential was E_{rev} = -80, 50 and

157 50 mV, for potassium, calcium and sodium respectively. Leak conductance reversal potentials

158 was -80 mV.

159

160 The conductance values were chosen based on their ability to induce a sufficient depolarization or
161 hyperpolarization of the resting membrane potential (approximately a 5 mV change) compared to the
162 passive model (g_K = 10 mS/cm², g_{Ca} = 0.1 mS/cm²). However, due to the explosive behavior of the
163 sodium current—which can induce a rapid and uncontrollable depolarization beyond the firing
164 threshold—we limited the sodium conductance to g_{Na} = 50 mS/cm², resulting in a depolarization of
165 approximately 1 mV (see Fig. 1). In some cases, we reduced the potassium conductance to 1 mS/cm²
166 to prevent complete silencing of spiking.
167
168 Models of A-type potassium, T-type calcium and transient sodium currents are a modified
169 version from Engbers et al. 2012; Jaffe et al. 1994; Korngreen et al. 2000; Dougalis et al. 2017;
170 and Hoffman et al. 1997. A-type potassium current equation is: $I_{kA} = g_{ak} n_{ka}^4 l_{ka}(V - E_K)$. T-
171 type calcium current equation is: $I_{CaT} = g_{CaT} {m_{CaT}}^2 h_{CaT}(V - E_{Ca})$. Transient sodium current
172 equation is: $I_{NaT} = g_{Na} m_{Na}^2 h_{Na}(V - E_{Na})$. Leak current equation is: $I_L = g_L(V - E_L)$.
173
174 In the next subsection, we describe how the simulations of these differential equations were
175 performed.
176
177 **Simulations**
178 Differential equations were solved using the Euler method and time step 0.05 ms. Synaptic
179 background activity was generated of evenly distributed 200 excitatory postsynaptic currents
180 (EPSCs) and 200 inhibitory postsynaptic currents (IPSCs) over time, to generate sparse or
181 synchronous synaptic backgrounds as found *in vivo* (Waters et al., 2006, Harris and Thiele
182 2011). EPSCs and IPSCs were generated using biexponential events: V_{Hold} = -50 mV, E_{AMPA} = 0
183 mV, E_{GABAA} = -60 mV and g = 0.1 nS. The time constants are $\tau_{\text{rise/AMPA}}$ = 1 ms, $\tau_{\text{decay/AMPA}}$ = 10

184 ms, $\tau_{rise/GABAA}$ = 2 ms, $\tau_{decay/\ GABAA}$ = 20 ms. For the synchronous case, we randomly removed
185 75% of the EPSCs and amplified the remaining ones by a factor of 4, with the goal of
186 reproducing a highly synchronous set of inputs.
187
188 We simulated theta oscillations at f = 4 Hz and analyzed four cycles of voltage traces using the
189 equation $I_\theta = Asin(2\pi ft)$, where A is the amplitude (5 μA/cm^2) and t is time in ms. Thus, we
190 injected in total the sum of the synaptic background activity with theta oscillations: $I_{inj} = I_{syn} +$
191 I_θ, in other words, the *in vivo*-like state was generated as the combination of synaptic
192 background activity with theta oscillations. We generated dendritic spikes using a leaky-integrate
193 and fire model with resting potential -60 mV and spiking threshold -40 mV.
194
195 In the next subsection, we will describe our procedure to determine how reduction/contraction or
196 amplification/prolongation occurs with the currents studied.
197
198 **Mathematical analysis of reducing/contracting and amplifying/prolonging currents**
199 Here we used an analytical approach to determine the effect of I_{KA}, I_{CaT}, and I_{NaT} on the input
200 resistance and membrane time constant. It is well known that τ_m is a function of I_i:
201 $$\tau_m = \frac{C}{\sum_{i=1}^{n} G_i}, \qquad \text{(Eq 5)}$$
202
203 where the input conductance G_i can be obtained by differentiating Eq.2:
204
205 $$G_i = \frac{\partial I_i}{\partial v} = \bar{g} p_i q_i + \bar{g}(V-E) q_i \frac{\partial p_i}{\partial v} + \bar{g}(V-E) p_i \frac{\partial q_i}{\partial v}. \qquad \text{(Eq 6)}$$
206

In this study all currents are inactivating. As shown in the results section (see Slow inactivation plays nearly no role on summation during *in vivo*-like states allowing for model reduction), all the inactivating currents produce similar voltage changes when it is assumed fast activation/inactivation kinetics. Under these circumstances, it is reasonable to assume $\tau_{act} = \tau_{inact} \rightarrow 0$. Consequently, p and q become functions of voltage alone, denoted as p = p(V) and q = q(V). In this state, they lose their time dependence and are solely voltage dependent. Specifically, $p = p^{\infty}(v)$ and $q = q^{\infty}(v)$. Therefore, when $\tau_{act} = \tau_{inact} \rightarrow 0$, Eq 6 can be expressed as:

$$\frac{\partial I_i}{\partial v} = \bar{g} p_i^{\infty} q_i^{\infty} + \bar{g}(V-E) q_i^{\infty} \frac{\partial p_i^{\infty}}{\partial v} + \bar{g}(V-E) p_i^{\infty} \frac{\partial q_i^{\infty}}{\partial v} \qquad \text{(Eq 7)}$$

$$\frac{\partial I_i}{\partial v} = \bar{g} p_i^{\infty} q_i^{\infty} + \bar{g}(V-E)\left(q_i^{\infty} \frac{\partial p_i^{\infty}}{\partial v} + p_i^{\infty} \frac{\partial q_i^{\infty}}{\partial v}\right). \qquad \text{(Eq 8)}$$

The term $\alpha = (V-E)\left(q_i^{\infty} \frac{\partial p_i^{\infty}}{\partial v} + p_i^{\infty} \frac{\partial q_i^{\infty}}{\partial v}\right)$ can assume positive or negative values. According to Eq. 5, when $\alpha > 0$, τ_m decreases and voltage changes are reduced, whereas when $\alpha < 0$, τ_m increases, and voltage changes are amplified. Currents with negative α are termed "amplifying/prolonging" as they lengthen τ_m, while those with a positive α are termed "reducing/contracting", as they shorten τ_m (Ceballos et al. 2017b).

The question arises: under what circumstances do the currents "amplify/prolong" or "reduce/contract"? To answer this, we need to investigate the conditions when α is positive or negative. We know that:

$$\frac{\partial p^{\infty}}{\partial v} > 0,\ \frac{\partial q^{\infty}}{\partial v} < 0,\ p^{\infty} > 0, \text{and}\ \ q^{\infty} > 0. \qquad \text{(Eq 9)}$$

Therefore, $q_i^{\infty}\frac{\partial p_i^{\infty}}{\partial v}$ is positive and $p_i^{\infty}\frac{\partial q_i^{\infty}}{\partial v}$ is negative. We also know that the membrane potential of dendrites typically ranges between -90 mV and +60 mV. The reversal potential for potassium (E_k) is usually assumed to be around -90 mV, while the reversal potential for sodium and calcium ($E_{Na,Ca}$) is assumed to be around +60 mV. Thus, for I_K ocurrs $V - E_k > 0$. Similarly, for I_{CaT} and I_{NaT}, V- $E_{Na,Ca}$ <0.

Substituting these into Eq. 7, we find that for I_K the first term is positive, the second is positive and the third is negative. Meanwhile, for I_{CaT} and I_{NaT}, the second is negative and the third is positive. This demonstrates that activation and inactivation have opposite effects on τ_m: one prolongs it while the other shortens it. This observation is consistent with the findings of Remme et al. (2011) and Richardson et al. (2003) that I_{KA} activation reduces, and inactivation amplifies the voltage scaling, and that I_{KA} activation shortens, and inactivation prolongs τ_m. Meanwhile, the opposite effect occurs for I_{CaT} and I_{NaT}.

A special case arises when inactivation is removed. This occurs for some voltage-dependent currents that exhibit either no inactivation or very slow inactivation (also known as nonactivating currents). This scenario can be simulated by setting q = 1. Therefore, we ask: when can $\alpha = (V - E)\frac{\partial p_i^{\infty}}{\partial v}$ be positive or negative, i.e., when does it contract or prolong τ_m, after inactivation is removed? We can easily deduce that, $(V - E_k)\frac{\partial p_i^{\infty}}{\partial v} > 0$ but $\left(V - E_{Na,Ca}\right)\frac{\partial p_i^{\infty}}{\partial v} < 0$. This

suggests that when removing the inactivation from I_{KA}, α is positive i.e., it is always a "contracting" current, meanwhile for I_{CaT} and I_{NaT} , α is negative i.e., it is always a "prolonging" current.

Results

Consistent membrane charging effects in the presence of potassium and sodium currents, but mixed response effects in the presence of calcium current

We begin our paper testing the effect of inactivating currents on membrane time constant (τ_m). For that, we built a single compartment dendritic model. We focused on the most relevant inactivating currents expressed in pyramidal neurons dendrites and activated near the spiking threshold: A-type potassium (I_{KA}), T-type calcium (I_{CaT}), and transient sodium (I_{NaT}) (see Methods). A depolarizing pulse of current was applied, and both exponential rise and decay followed by this pulse were analyzed. Fig. 1A shows that I_{KA} hyperpolarizes the resting membrane potential, reduces the amplitude of the response, and accelerates the capacitor's charge. In contrast, I_{NaT} amplifies the response amplitude and slows down the capacitor's charge but has no effect on the resting membrane potential due to its activation at higher membrane potentials (Fig 1B).

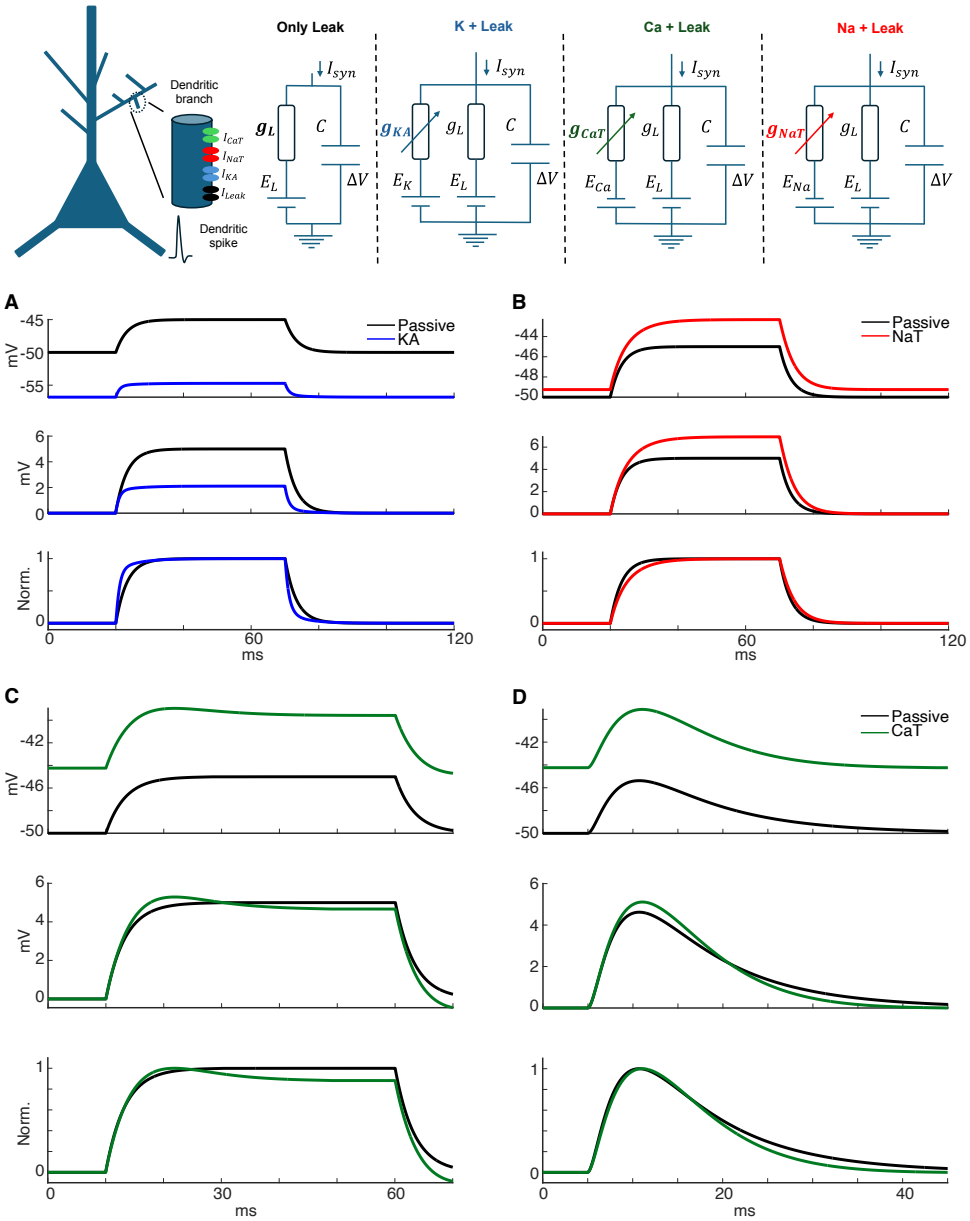

Fig 1. Membrane charging in the presence of the different ionic currents. Sketch at the top represents the four single dendritic branch models used in the simulations: Only leak (or passive, black), leak plus potassium current (blue), leak plus calcium current (green) and leak plus sodium current (red). In panels A, B, C and D, a current pulse of 50 ms was injected and the voltage change is displayed in the plots that are organized as: the original voltage trace of the relevant current plus leak model (coloured) and passive model (black) (upper), after baseline subtraction (middle), and after normalization (bottom). A. Voltage trace of the model with leak current plus I_{KA}. B. Voltage trace of the model with leak current plus I_{NaT}. C.

Voltage trace of the model with leak current plus I_{CaT}. D. An excitatory synaptic current was injected and the voltage changes are displayed in the plot that is organized as: the original voltage trace of the I_{CaT} plus leak current model (coloured) and passive model (black) (upper), after baseline subtraction (middle), and after normalization (bottom). In the simulations, the initial resting membrane potential is -50 mV. The conductance values were: $g_{KA} = 10$, $g_{CaT} = 0.1$ and $g_{NaT} = 50$, respectively. EPSCs were generated using biexponential events: $E_{rev} = 0$ mV, $g = 0.04$ nS. The time constants are $\tau_{rise} = 1$ ms, $\tau_{decay} = 10$ ms.

Opposed to this pattern, the effects of I_{CaT} were mixed. I_{CaT} depolarizes the resting membrane potential. However, there is only amplification of the voltage change at the onset of the current pulse, while there is a reduction of the voltage change at the end of the pulse due to slow inactivation kinetics (Fig 1C). We also observed a clear phase delay during the rising phase of the EPSP (excitatory postsynaptic potential), but the decay phase showed mixed behavior, starting with a phase delay in one direction and eventually reversing its direction (Fig 1D). We believe this mixed behavior in amplification/reduction of the voltage change and lengthening/shortening of the voltage provides insight into the inconsistent reports found in the literature about I_{CaT} (Stuart et al. 1995; González-Burgos et al. 2001; Andreasen et al. 1999; Hsu et al. 2018; Seong et al. 2014, Fukaya et al. 2018; Gillessen et al. 1997, Prescott et al. 2005, Liu et al. 2008; Connelly et al. 2016; Urban et al. 1998; Evans et al. 2017; Deleuze et al. 2012).

Moreover, we further investigated the combined effects of multiple ionic currents (I_{KA}, I_{CaT} and I_{NaT}) by measuring the difference in resting membrane potentials (ΔRMP), scaling, and the membrane time constant (τ_m). In the heatmaps presented in Fig. S1, two conductance values were varied while one was fixed, allowing us to assess how the combination of these currents influences these measures. ΔRMP was calculated as the difference between the RMPs of the two traces, while

300 scaling was determined as the ratio of the voltages (V_2/V_1). The membrane time constant was
301 obtained by fitting the rising phase with a single exponential function. The results from this
302 supplementary figure demonstrate a strong correlation between scaling and τ_m, which is expected
303 based on the mathematical relationship $\tau_m = R_{input} \times C_m$, where scaling is analogous to the
304 traditional input resistance. Furthermore, in the presence of the other currents, I_{KA} decreases τ_m,
305 whereas I_{CaT} and I_{NaT} increase τ_m. Notably, I_{CaT} has a mild effect on τ_m but a strong effect on the
306 resting membrane potential.
307
308 **Voltage changes scaling monotonically during theta oscillations**
309 The previous section studied the effect of the inactivating currents on the temporal properties of
310 a dendritic model. The model was stimulated using simple current pulses and simulated EPSPs.
311 Here, we wondered whether the previous results also apply under *in vivo*-like conditions. Here,
312 we investigated the effects of the inactivating currents on scaling voltage traces from *in vivo*-like
313 conditions. We injected synaptic currents, consisting of evenly distributed EPSCs and IPSCs
314 over time, to generate sparse synaptic backgrounds as found *in vivo* (Waters et al. 2006). To add
315 realistic background to the synaptic currents, we simulated theta oscillations at 4 Hz and
316 analyzed four cycles of voltage traces (Fig. 2; cycles identified by different colors). Our results
317 show that I_{KA} causes a negative shift of the voltage changes (Fig 2A), whereas I_{CaT} and I_{NaT}
318 cause a positive shift (Fig 2C, 2E). The scaling from above -60 mV is linearly correlated with the
319 membrane voltage for I_{KA} and I_{NaT} (Fig 2B, 2F) but no clear tendency is found for I_{CaT}, only high
320 variability (Fig 2D). The data presented in Fig. 2 reveal that I_{KA} induces a negative shift with
321 scaling at approximately 90% at the peak of a cycle, whereas I_{NaT} causes a positive shift with
322 scaling at around 115%. When translated to voltage, this corresponds to a shift of approximately

6 mV. Given that we are operating in a regime near the action potential threshold and considering the context of an *in vivo*-driven neuron, this shift can be decisive in determining whether a spike occurs. These findings indicate that I_{KA} and I_{NaT} can modulate spiking activity in an oscillatory state, highlighting the significance of these currents in shaping neuronal excitability.

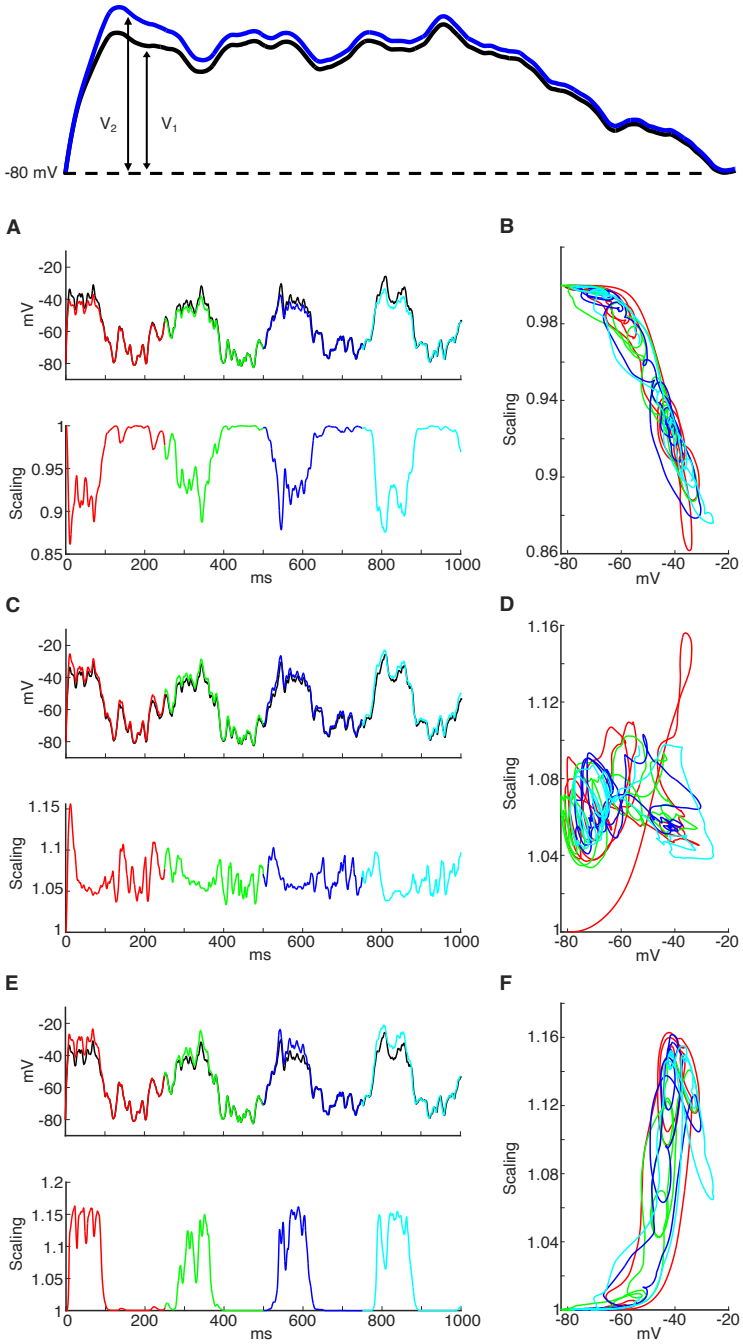

Fig 2. Sketch of voltage traces and the measurement of the relative voltage used to calculate the scaling. Voltage changes for dendritic ionic currents under *in vivo*-like conditions. Dendritic models were stimulated by injection of a 4 Hz theta oscillations plus synaptic background made of randomly distributed excitatory and inhibitory synaptic currents. The plot displays the voltage traces of the passive dendrite (black solid line). Red/Green/Blue/Cyan represent first to fourth cycle of the theta sequence in

335 the dendrite models with leak current plus the relevant ionic current. A. Voltage traces and scaling of
336 dendrite expressing only leak current plus I_{KA}. B. phase plot of nonlinear scaling vs membrane potential.
337 C. Voltage traces and scaling of dendrite expressing only leak current plus I_{CaT}. D. phase plot of nonlinear
338 scaling vs membrane potential. E. Voltage traces and scaling of dendrite expressing only leak current plus
339 I_{NaT}. F. phase plot of nonlinear scaling vs membrane potential. Scaling was defined as $(V_2 + 90) / (V_1 +$
340 $90)$, where V_2 is the voltage trace of the neuron model with both leak and relevant currents, and V_1 is the
341 voltage trace with only the leak current. Since the lowest simulated voltage is -80 mV, we added 90 mV
342 to ensure all values remain positive. Phase plots are showing the voltage-dependence of the scaling. This
343 is an analogous measurement of the conventional way to investigate the amplification/shrinking of EPSPs
344 by voltage-dependent currents found in in vitro studies. The conductance values were: $g_{KA} = 1$, $g_{CaT} = 0.1$
345 and $g_{NaT} = 50$, respectively.
346
347 Fig 3 shows the nonlinear scaling for input frequency oscillations from 1 to 30 Hz. The set of
348 Figs 3A-C demonstrate a clear difference in the voltage scaling when comparing the ionic
349 currents. More specifically, we observed a consistent decrease for I_{KA} across depolarizing
350 voltages and a consistent increase for I_{NaT} across depolarizing voltages (see heatmaps in Fig 3D
351 and Fig 3F). In contrast, I_{CaT} showed nonmonotonic behavior of the scaling for low frequencies,
352 but monotonic for high frequencies (Fig 3E). Then we evaluated the behavior of the scaling for
353 different conductance values at 4 Hz. We observed a consistent decrease for I_{KA} across
354 depolarizing voltages and a consistent increase for I_{NaT} across depolarizing voltages (Fig 3G and
355 Fig 3I). In contrast, I_{CaT} showed similar values across voltage (horizontal lines, Fig 3H).
356

These results suggest that most of the knowledge from Fig 1 can be transferred to the *in vivo*-like states except for I_{CaT}, where its ionic currents scale the voltage differently in a frequency-dependent manner.

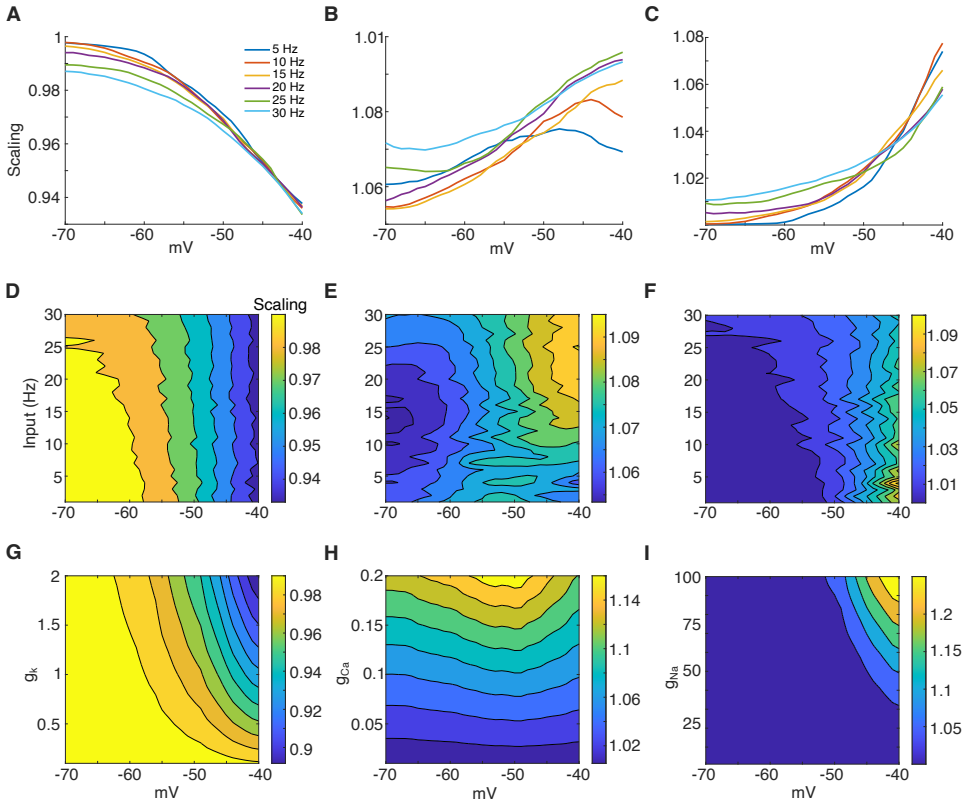

Fig 3. Frequency and ionic effect on voltage scaling. The nonlinear scaling is computed when input frequency oscillations change range from 1 to 30 Hz. A. Curves for added I_{KA}. B. Curves for added I_{CaT}. C. Curves for added I_{NaT}. D. Heatmap of the nonlinear scaling for voltages from -70 to -40 mV vs. input frequency oscillations change from 1 to 30 Hz for I_{KA}. E. Same as in D but for I_{CaT}. F. Same as in D but for I_{NaT}. G. Heatmap of nonlinear scaling for voltages from -70 to -40 mV vs. I_{KA} conductance. $g_{CaT} = 0.1$ and $g_{NaT} = 50$. H. Same as in G but for I_{CaT} conductance. $g_{KA} = 1$ and $g_{NaT} = 50$. I. Same as in G but for I_{NaT} conductance. $g_{KA} = 1$ and $g_{CaT} = 0.1$. Frequency was fixed at 4 Hz for G, H and I plots. Scaling was defined as $(V_2 + 90) / (V_1 + 90)$, where V_2 is the voltage trace of the neuron model with both leak and

370 relevant currents, and V_1 is the voltage trace with only the leak current. Since the lowest simulated
371 voltage is -80 mV, we added 90 mV to ensure all values remain positive. The conductance values were:
372 $g_{KA} = 1$, $g_{CaT} = 0.1$ and $g_{NaT} = 50$, respectively.
373

374 **Changes in activation are linearly correlated with changes in inactivation for T-type**
375 **calcium and A-type potassium currents**

376 We previously observed the effect of the inactivating currents on the scaling of the voltage. I_{KA}
377 and I_{NaT} showed linear correlation with voltage, but no consistent tendency was observed for
378 I_{CaT}. In this section, to investigate the biophysical mechanisms underlying these discrepancies we
379 present phase plots of activation versus inactivation variables for theta oscillations (Fig. 4). This
380 analysis demonstrated a clear negative correlation, where increases in activation correspond with
381 decreases in inactivation (Fig 4G, 4H, 4J and 4K). Interestingly, the window current properties of
382 I_{NaT} are markedly different than I_{KA} and I_{CaT} and produced a highly nonlinear correlation
383 between activation and inactivation variables, where large values of one variable correlate with
384 small values of the other (Fig 4I). We verified that this relationship is well-fitted by a power law
385 function (Fig 4L).
386

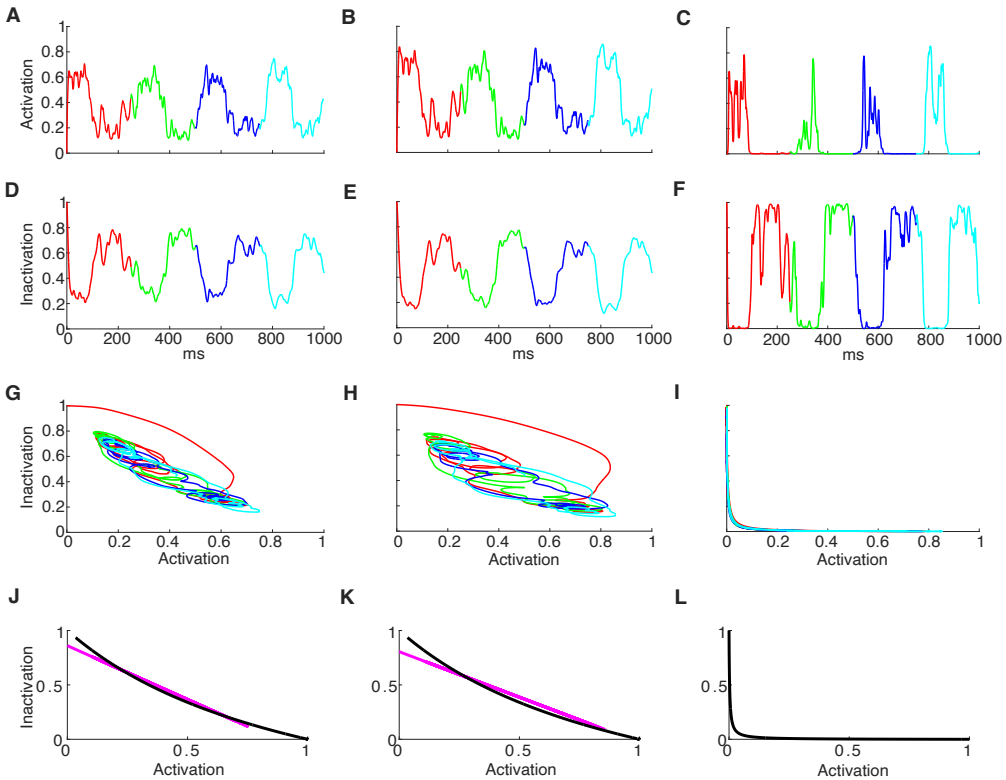

Fig 4. Activation vs. inactivation functional relationships. A-F. The curves represent activation and inactivation variables under 4 Hz theta oscillations. Red/Green/Blue/Cyan represent first to fourth cycle of the theta sequence with the added ionic current: activation for A. I_{KA}. B. I_{CaT}. C. I_{NaT}; inactivation for D. I_{KA}. E. I_{CaT}. F. I_{NaT}. G-I: Phase plots of activation vs inactivation for G. I_{KA}. H. I_{CaT}. I. I_{NaT}. Notice the filtering of the inactivation variable due to the slow inactivation kinetics of I_{CaT} and I_{KA}. J-L: Linear fitting of activation vs. inactivation phase plots for J. I_{KA}. K. I_{CaT} (magenta) and power-law fitting for L. I_{NaT}. Trajectories when $\tau_{act} = \tau_{inact} = 0$ (black). The conductance values were: $g_{KA} = 1$, $g_{CaT} = 0.1$ and $g_{NaT} = 50$, respectively.

Analysis of the activation vs. inactivation phase plots showed that fitting trajectories of I_{KA} and I_{CaT} by a linear regression returns a curve very similar to the trajectories when $\tau_{act} = \tau_{inact} = 0$ (Fig

399 4J and 4K). This allows us to approximate the functional relationship between activation or
400 inactivation. Therefore, we use the linear regression to substitute the inactivation variable by a
401 linear function dependent on the activation variable: $q_{Inact} = - p_{Act} + 0.85$ for I_{KA} and, $q_{Inact} = -$
402 $0.84p_{Act} + 0.8$ for I_{CaT}. In contrast, the trajectories for I_{NaT} are highly nonlinear and, as explained
403 above, were fitted using a power law function with 4/3 exponent ($q_{Inact} = 10^{-3} {p_{Act}}^{-4/3}$) (Fig 4I
404 and 4L). This functional behavior is the result of the way activation and inactivation curves
405 interact within the window current.
406
407 Our results showed similar activation/inactivation linear trajectories for I_{KA} and I_{CaT}, although
408 these two currents differ in their inactivation kinetics (e.g. $\tau_{inact} = 5$ ms for I_{KA} but 10 ms for I_{CaT}).
409 This suggests that under *in vivo*-like conditions, voltage changes are robust to inactivation
410 kinetics.
411
412
413 **Slow inactivation plays nearly no role on summation during *in vivo*-like states**
414 Based on the results above, we interrogate whether *in vivo*-like states require kinetics. Therefore,
415 we investigated whether we could get similar voltage traces when using the actual kinetics vs.
416 when using fast kinetics, i.e. $\tau_{act} = \tau_{inact} = 0.1$ ms. Surprisingly, for all simulated currents we
417 obtained traces that were similar with average differences less than 0.6 mV for voltages below
418 spiking threshold (V = -40 mV; Fig 5D). These results suggest that the system of equations can
419 be reduced when assuming $\tau_{act} = \tau_{inact} = 0$, hinting that the dynamics provided by Eq 3 is no
420 longer necessary for *in vivo*-like conditions. Suprathreshold spiking activity also displayed
421 similar results (Fig S2).

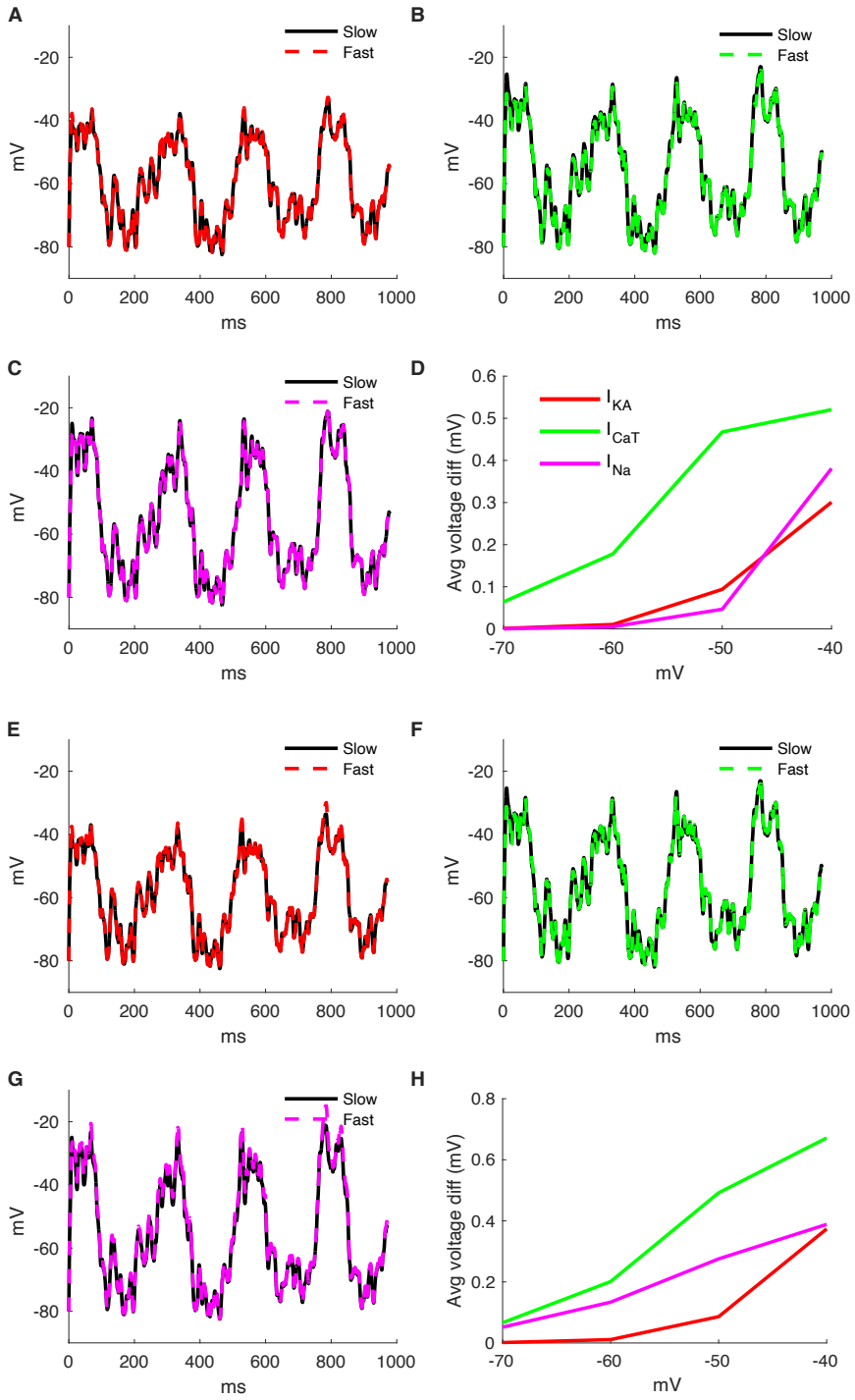

Fig 5. Comparison of traces using actual kinetics vs. fast kinetics (i.e. $\tau_{act} = \tau_{inact} = 0.1$ ms). A. I_{KA}. B. I_{CaT}. C. I_{NaT}. D. Average voltage difference between the two tested conditions (I_{KA} in red, I_{CaT} in green, I_{NaT} in magenta). Comparison of traces using actual activation/inactivation variables and kinetics vs. fast kinetics

426 (i.e. $\tau_{act} = \tau_{inact} = 0$ ms) and after linearizing inactivation variables using activation variable for I_{KA} and
427 I_{CaT} and power law approximation for I_{NaT}. E. I_{KA}. F. I_{CaT}. G. I_{NaT}. H. Average voltage difference between
428 the two tested conditions (I_{KA} in red, I_{CaT} in green, I_{NaT} in magenta). The conductance values were: g_{KA} =
429 1, g_{CaT} = 0.1 and g_{NaT} = 50, respectively.
430
431 Further, and following the relationships from the previous section, we can also reduce the
432 inactivation variable using the linear relation obtained from the linear regression above for I_{KA}
433 and I_{CaT} and power law approximation for I_{NaT} inactivation. As a result of all the reductions, we
434 can express the behavior of each current as dependent on only a single activation variable.
435 Therefore, we use the linear regression to substitute the inactivation variable by a linear function
436 dependent on the activation variable for I_{KA} and I_{CaT} and power law approximation for I_{NaT}. We
437 also consider $\tau_{act} = \tau_{inact} = 0$. Fig 5H demonstrates that this approximation can obtain similar
438 voltage traces with average values below 0.7 mV for all currents.
439
440 The results from this section allowed us to reduce the dendrite system of equations to a single
441 variable that resolves the activation variable only. Our approximation is akin to the Morris-Lecar
442 reduction (Izhikevich 2007). However, in our case, the assumption of instantaneous kinetics
443 allows us to avoid coupling differential equation.
444
445 In the next set of experiments, we wondered about the dependency of our results with the input
446 frequency. Fig 6 shows the voltage difference between the model with slow kinetics vs.
447 instantaneous for input frequency oscillations from 1 to 30 Hz. We observed a consistent
448 increase for all currents across depolarizing voltages, with values below 0.7 mV for I_{KA}, 1.2 mV
449 for I_{CaT} and 0.35 mV for I_{NaT} (Fig 6D, 6E and 6F). Then we evaluated the voltage difference

between the model with slow kinetics vs. instantaneous kinetics for different conductance values with input frequency fixed at 4 Hz. We observed a consistent increase for all currents across depolarizing voltages, with lowest values at conductance close to g_{KA} = 1, g_{CaT} = 0.1 and g_{NaT} = 50 (Fig 6G, 6H and 6I).

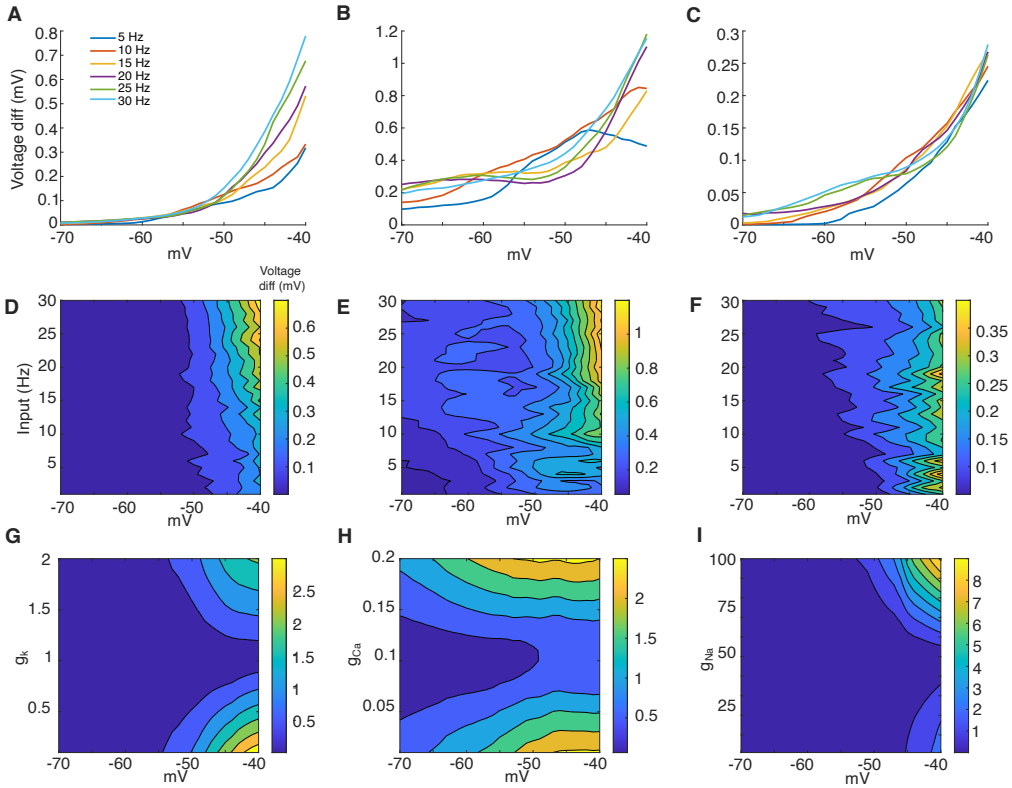

Fig 6. Voltage difference between the model with slow kinetics vs. instantaneous, when input frequency oscillations change from 1 to 30 Hz. A. I_{KA}. B. I_{CaT}. C. I_{NaT}. D. Heatmap of voltage difference between the model with slow kinetics vs instantaneous for voltages from -70 to -40 mV vs. input frequency oscillations change from 1 to 30 Hz for I_{KA}. E. Same as in D but for I_{CaT}. F. Same as in D but for I_{NaT}. G. Heatmap of the voltage difference between the model with slow kinetics vs instantaneous for voltages from -70 to -40 mV vs. I_{KA} conductance. g_{CaT} = 0.1 and g_{NaT} = 50. H. Same as in D but for I_{CaT}

conductance. g_{KA} = 1 and g_{NaT} = 50. I. Same as in D but for I_{NaT} conductance. g_{KA} = 1 and g_{CaT} = 0.1. The conductance values were: g_{KA} = 1, g_{CaT} = 0.1 and g_{NaT} = 50, respectively.

These results suggest that the voltage differences between the model with slow kinetics and fast kinetics is independent of the frequency input, but dependent on the voltage. As to the latter, as the depolarization became stronger, the voltage difference identified grew greater, showcasing that the kinetics becomes more prominent as the voltage gets closer to the threshold of the neuron.

Inactivation opposes activation effects on voltage scaling and membrane time constant

We know from above that activation and inactivation have negative correlation, but it is still unknown how this correlation determines the voltage scaling and temporal properties of the voltage traces in the presence of I_{KA}, I_{CaT} and I_{NaT}. On the other hand, it is well known that scaling is inversely related to the input conductance and that the temporal properties are related to the membrane time constant. We first used an analytical approach to determine the opposed effect of the inactivation on voltage scaling and temporal properties compared to activation. When comparing the input conductance for inactivating current (as shown in Eq 8) vs non-inactivating current (as shown in Eq 10), we know from Eq 9 that $p_i^\infty q_i^\infty < p_i^\infty$ and $q_i^\infty \frac{\partial p_i^\infty}{\partial v} + p_i^\infty \frac{\partial q_i^\infty}{\partial v} < \frac{\partial p_i^\infty}{\partial v}$. Thus, input conductance of inactivating currents is always smaller compared to the non-inactivating case, suggesting that the effect of inactivation is always to oppose to the activation.

To test the opposite effects of activation and inactivation, we investigated the temporal summation of a train of 3 EPSPs separated by 10 ms. We tested the effect of the inactivating current and their respective non-inactivating version (Fig 7). These conditions are represented by the following equations: current with inactivation ($I_i = \bar{g}_i p_i q_i (V - E_{rev}^i)$), and current without inactivation or non-inactivating ($q_i = 1$, thus, $I_i = \bar{g}_i p_i (V - E_{rev}^i)$). The plots show that noninactivating currents enhance the effect compared to their inactivating counterpart. These results suggest that inactivation counteracts the effect of the activation, reducing its effect.

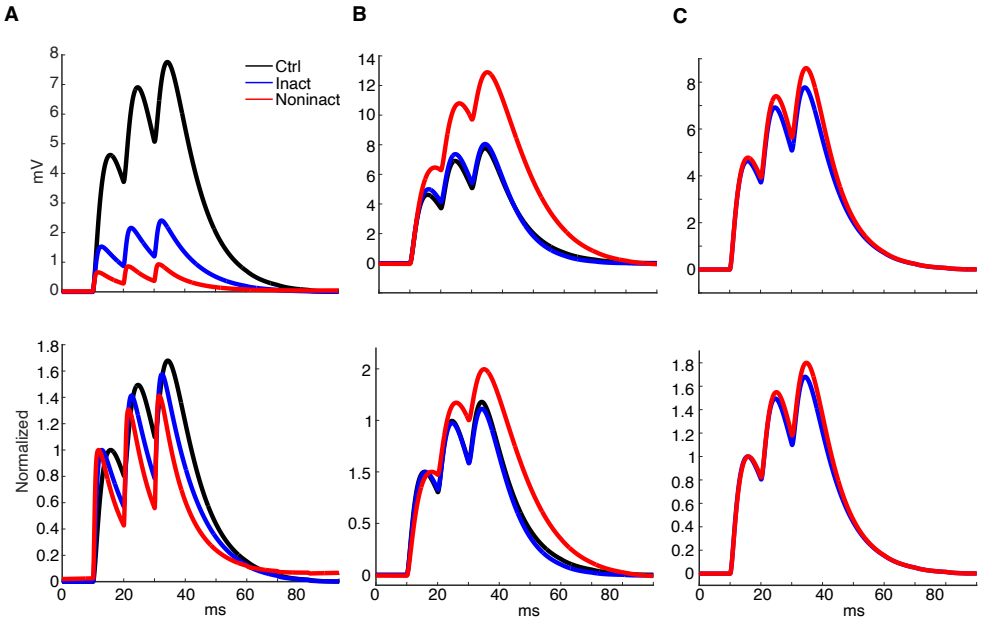

Fig 7. Inactivation and activation effects on summation. The voltage traces show summation for a train of 3 excitatory synaptic potentials at 100 Hz. A. Model with I_{KA}. B. Model with I_{CaT}. C. Model with I_{NaT}. Initial resting membrane potential is -50 mV. Top: after baseline subtraction, bottom: after normalization. Three conditions were analyzed: only leak current (black), leak + inactivating current (blue), leak + noninactivating current (red). These conditions are represented by the following equations: current with inactivation ($I_i = \bar{g}_i p_i q_i (V - E_{rev}^i)$), and current without inactivation or non-inactivating

500 ($q_i = 1, thus, I_i = \bar{g}_i p_i(V - E^i_{rev})$). EPSCs were generated using biexponential events: E_{rev} = 0 mV, g =

501 0.04 nS. The time constants are τ_{rise} = 1 ms, τ_{decay} = 10 ms. The conductance values were: g_{KA} = 10, g_{CaT} =

502 0.1 and g_{NaT} = 0.5, respectively.

503

504 While in this section we showed that inactivation opposes activation effects on voltage scaling

505 and membrane time constant with analytical derivations, together with previous sections we can

506 conclude that I_{KA} activation shortens τ_m whereas inactivation prolongs it (Fig 7A). Meanwhile,

507 an opposite effect occurs for I_{CaT} and I_{NaT} (Fig 7B and 7C). Together, these observations have

508 profound implications for dendritic computation, in particular to their temporal summation

509 properties. In the next section, we will show how our results are useful to study synchrony- vs.

510 rate-code.

511

512

513 **A-type potassium current enhances synchrony-code but T-type calcium and transient**

514 **sodium currents enhance rate-code**

515 Temporal summation of synaptic potentials can be used to identify integrators or coincidence

516 detector neurons. Integrators, characterized by a long τ_m, allow summation of synaptic potentials

517 even when they occur far apart in time. In contrast, coincidence detectors, with a short τ_m,

518 integrate synaptic potentials only when they occur closely together in time. Previous studies have

519 shown the association between high expression of potassium currents and coincidence detection

520 mode, and high expression of calcium/sodium currents and integration mode (Mathews et al.

521 2010; Branco et al. 2016). We tested this hypothesis using an analytical approach to demonstrate

522 that for instantaneous inactivating currents, potassium currents such as I_{KA} always decrease the

523 input resistance and shorten the membrane time constant, meanwhile calcium/sodium currents

524 such as I_{CaT}, and I_{NaT} always increase the input resistance and prolong the membrane time
525 constant (see Methods, section Mathematical analysis of reducing/contracting and
526 amplifying/prolonging currents).
527
528 Moreover, coincidence detection and integration on the level of dendritic compartments can be
529 seem translated to synchrony-code and rate-code on the level of network computations, with
530 coincidence detectors being more likely to fire with synchronized inputs and poorly integrate
531 sparse inputs. In contrast, integrators can summate sparse inputs to generate dendritic spikes but
532 respond less to coincident inputs compared to coincidence detectors. Thus, a natural question we
533 investigate in this section is how the modulation of the I_{KA}, I_{CaT} and I_{NaT} affect the synchrony vs.
534 rate-code.
535
536 Accordingly, we randomly generated 100 sparse and 100 synchronous input currents and used
537 them to generate 100 voltage traces also stimulated by theta input (4 Hz). The sparse and
538 synchronous input were developed to create distinction between these codes (synchrony- vs.
539 rate-code). Both sparse and synchronous inputs had the same amount of 200 EPSCs and 200
540 IPSCs randomly distributed in the course of a simulation. For the synchronous case, we removed
541 randomly 75% of the EPSCs and the remaining were amplified by a factor of 4 with the rationale
542 of reproducing a highly synchronous set of inputs.
543
544 While a consistent decrease in firing occurs in the presence of the I_{KA} (compare Fig 8A to B), an
545 increase in firing occurs for I_{CaT} and I_{NaT} (compare Fig 8A to C and D). This aligns with the
546 shrinkage and amplification of voltage changes seen above. When all three currents were

present, firing rates remained unchanged (not shown), indicating that the effects of I_{KA} were counteracted by I_{CaT} and I_{NaT} as expected. The figure demonstrates the ability of ionic currents to transform a neuron into a coincident detector that is more likely to process synchronized inputs and less likely to integrate sparse inputs. This is the case for I_{KA}, as it more effectively processes synchronous inputs (see histograms in Fig. 8F). The other currents do not exhibit this ability, processing synchronous and sparse inputs equally.

To further quantify our results in Fig. 8, we require a metric that can determine the preferred synaptic summation mode (coincidence vs. integration). Thus, we calculated the relative change in spiking frequency of a dendrite when presented with sparse versus synchronized synaptic inputs ($\% \, relat \, freq_i = 100 \frac{(freq_i^{sync} - freq_i^{sparse})}{freq_i^{sparse}}$), where $freq_i^{sync}$ is the spiking frequency when stimulated with synchronized input and $freq^{sparse}$ is the spiking frequency when stimulated with sparse input. *i* is the corresponding relevant current (I_{KA}, I_{CaT} or I_{NaT}). We expect that coincidence detectors will show an increase in relative spiking frequency, while integrators will show a decrease. We tested this new metric in a single passive compartment dendrite model by changing the conductance value or capacitance density (Fig S3). The heatmap shows the percentage of relative frequency change when dendrites were stimulated using sparse vs synchrony input. We used this index (% relative frequency) as a measure of the strength of the preferred neural code mode employed by the dendrite. For instance, % relative frequency of 100% suggests the dendrite acts as a perfect coincident detector, meanwhile 0% suggests the dendrite acts as a perfect integrator. According to the values obtained from the index, we found that the dendrite would act closer to a perfect integrator when g_{Leak} was low or when capacitance density was high, both conditions consistent with long τ_m.

As shown in Fig 8, synchronous input increases firing rate. The relative increase in frequency is highest at the onset of the rise and decay of the theta cycle and lowest at the peak (Fig 8E, 8F, 8G and 8H). The exception is the potassium current where no large relative increase was observed at the decay (Fig 8F). We also calculated the relative difference of frequency between sparse vs synchronous stimulation (Fig 8E, 8F, 8G and 8H). We found a significant increase in the presence of I_{KA} relative to the passive dendrite (17.44 ± 1.38 % for passive, 38.86 ± 4.65 % for I_{KA}, $p < 0.001$). We also found a significant decrease in the presence of I_{CaT} and I_{NaT} relative to the passive dendrite (9.77 ± 0.81 % for I_{CaT}, 10.53 ± 0.8 % for I_{NaT}, $p < 0.001$). Also, I_{KA} was significantly higher than I_{CaT} and I_{NaT} ($p<0.001$). Finally, I_{CaT} and I_{NaT} were not significantly different ($p = 0.5$). These results suggest that I_{KA} enhances synchrony-code, while I_{CaT} and I_{NaT} enhance rate-code.

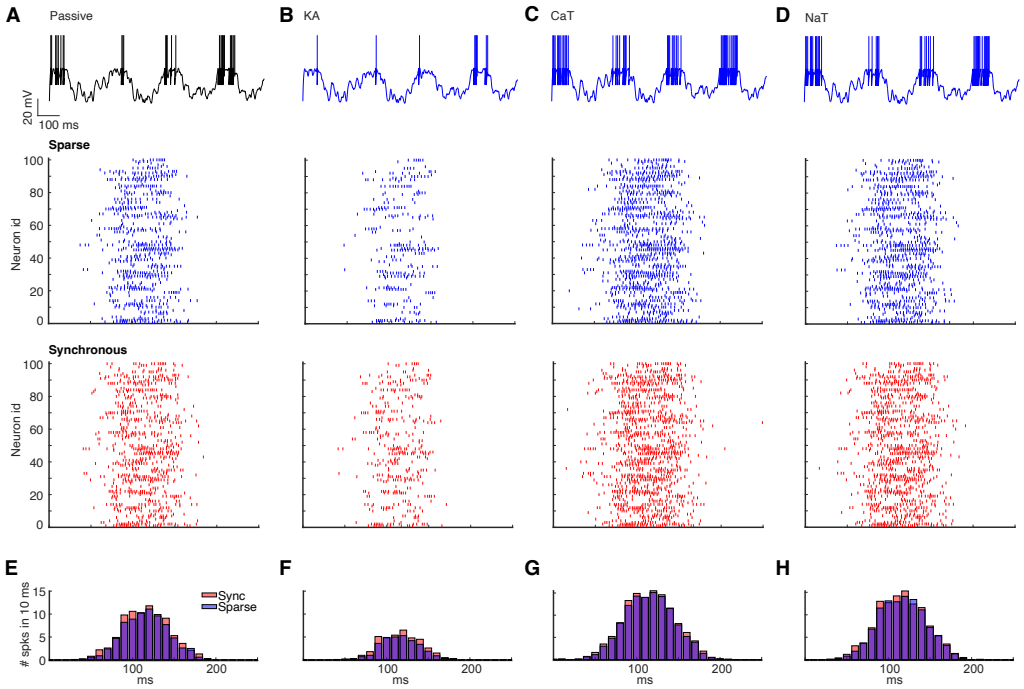

583

584 Fig 8. Synchrony- vs. rate-code and ionic currents dependency. Every column in the figure contains an
585 exemplary voltage trace followed by raster plots of the sparse and synchronous inputs, as well as a post-
586 stimulus time histogram (PSTH). Firing pattern under 4 Hz theta oscillations in a dendrite expressing. A.
587 only leak current. B. dendrite expressing only leak current plus I_{KA}. C. neuron expressing only leak
588 current plus I_{CaT}. D. dendrite expressing only leak current plus I_{NaT}. (E, F, G, H). The figure demonstrates
589 the ability of ionic currents to transform a neuron into coincident detector which is more likely to process
590 synchronized inputs and less integrate sparse inputs, which is the case of I_{KA}. The conductance values
591 were: $g_{KA} = 1$, $g_{CaT} = 0.1$ and $g_{NaT} = 50$, respectively.

592

593 We then expand our analysis to investigate the tuning range of specific neural code modes and
594 how they depend on the conductance values of I_{KA}, I_{CaT} and I_{NaT}. We use the same dendritic
595 model used above, but now we added all 3 currents to the model, while changing their
596 conductance values selectively. According to the values obtained from the index, we found that

the dendrite would act closer to a perfect integrator when g_{KA} was low (Fig 9A) or when g_{CaT}/g_{NaT} were high (Fig 9H, I). Under these conditions, the variability of the other conductances did not affect much the index value (the heatmaps are blueish). These results suggest I_{KA} is responsible for changing the dendrite to a more coincidence detection mode meanwhile I_{CaT} and I_{NaT} take the dendrite closer to an integration mode. This can also be observed for high values of g_{KA} (see Fig 9G) or when g_{CaT}/g_{NaT} is low (Fig 9B, C). Under these conditions the variability of the other conductances play a significant role that affects the index value (the heatmaps change from dark blue to light yellow).

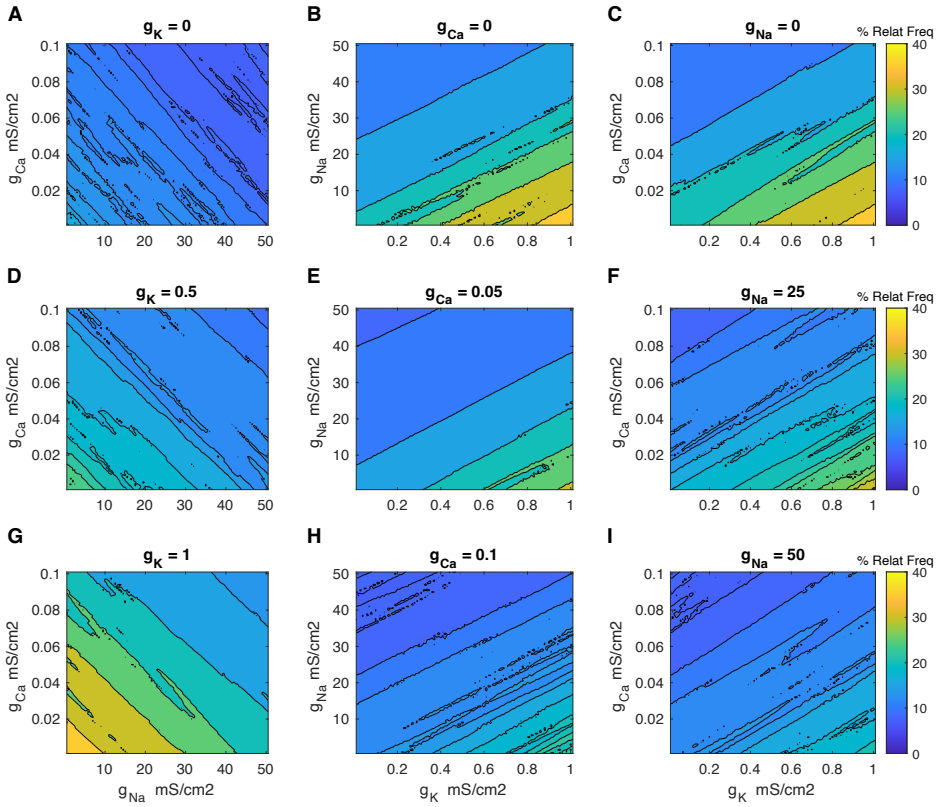

Fig 9. Heatmaps of % relative frequency (% relat freq) computed as difference between the sparse versus synchronized synaptic inputs spanned over different conductance values (see axis). Firing pattern under 4 Hz theta oscillations stimulation. A. g_{NaT} vs g_{CaT} when $g_K = 0$. B. g_{KA} vs g_{NaT} when $g_{Ca} = 0$. C. g_{KA} vs g_{CaT}

610 when $g_K = 0$. D. g_{NaT} vs g_{CaT} when $g_K = 0.5$. E. g_{KA} vs g_{NaT} when $g_{Ca} = 0.05$. F. g_{KA} vs g_{CaT} when $g_{Na} = 25$.
611 G. g_{NaT} vs g_{CaT} when $g_K = 1$. H. g_{KA} vs g_{NaT} when $g_{Ca} = 0.1$. I. g_{KA} vs g_{CaT} when $g_{Na} = 50$. Notice that the
612 dendrite would act closer to a perfect integrator when g_{KA} was low or when g_{CaT}/g_{NaT} were high,
613 suggesting that I_{KA} is responsible for changing the dendrite to a more coincidence detection mode
614 meanwhile I_{CaT} and I_{NaT} take the dendrite closer to an integration mode. This can also be observed for
615 high values of g_{KA} or when g_{CaT}/g_{NaT} is low. The % relative frequency is an indicator of whether the
616 dendrite acts as an integrator of coincidence detector (100% for perfect coincident detector and 0% for
617 perfect integrator). $\%\, relative\ frequency_i = 100\frac{(freq_i^{sync} - freq_i^{sparse})}{freq_i^{sparse}}$, where $freq_i^{sync}$ is the spiking
618 frequency when stimulated with synchronized input and $freq^{sparse}$ is the spiking frequency when
619 stimulated with sparse input. i is the corresponding relevant current (I_{KA}, I_{CaT} or I_{NaT}).
620
621 Overall, the results from Fig. 9 show a relative frequency below 40%, suggesting that under the
622 investigated conditions, the dendrite mainly behaves as an integrator.
623
624 **Discussion**
625 This study examines an important aspect of the neural coding by focusing on different modes of
626 *in vivo* dendritic synaptic integration. We show the role of inactivating currents on dendritic
627 temporal properties, and how the modes vary from integration of synaptic potentials over time
628 (long τ_m) to coincidence detection of closely timed potentials (short τ_m) (Mathews et al. 2010;
629 Prescott and De Koninck 2005; Ceballos et al. 2018; Farries et al. 2010; Branco et al. 2016).
630
631 Our results point to the role of A-type potassium currents in shortening τ_m, while T-type calcium
632 and transient sodium currents lengthen it, similar to non-inactivating currents. This suggests
633 inactivation reduces current strength without altering its profile. Additionally, activation and

634 inactivation affect τ_m in opposite ways, with currents that shorten τ_m upon activation prolonging
635 it upon inactivation and vice versa, consistent with previous studies (Richardson et al. 2003).
636 These findings also apply to fast-activating, non-inactivating currents, e.g. M-type potassium and
637 persistent sodium currents.
638
639 In terms of firing, we found that A-type potassium currents consistently reduce firing rates,
640 whereas T-type calcium and transient sodium currents increase them. This is due to potassium
641 currents hyperpolarizing the membrane, reducing voltage amplitude, and shortening temporal
642 changes, which decreases excitability. In contrast, calcium and sodium currents depolarize the
643 membrane, enhance voltage amplitude, and extend temporal changes, thereby increasing
644 excitability.
645
646 In relation to the effects of inactivating currents under *in vivo*-like conditions with oscillatory
647 inputs and synaptic fluctuations, both I_{KA} and I_{NaT}, were observed scaling changes above -60
648 mV, showing monotonic trends with variability. The rise and decay phases followed distinct
649 pathways, indicating that these currents differentiate between depolarization and
650 hyperpolarization. No clear trend was found for I_{CaT}, but its amplification pattern remained.
651
652 Activation and inactivation trajectories were linearly correlated for I_{KA} and I_{CaT}, but nonlinear for
653 I_{NaT}, independent of kinetics. Surprisingly, activation/inactivation kinetics had minimal impact
654 on voltage changes, with differences of less than 1 mV, suggesting potential misinterpretations
655 when extrapolating *in vitro* data to *in vivo* contexts. This underscores the importance of *in vivo*

656 recordings to fully understand dendritic behavior (Moore et al. 2017; Ujfalussy et al. 2018;
657 Dembrow et al. 2022; Liao et al. 2024).
658
659 We can regard our results as a step towards understanding how dendrites process information. In
660 particular, we have also tested temporally distinct patterns. Synaptic summation in the presence
661 of A-type potassium currents promoted firing with synchronized input, while T-type calcium and
662 transient sodium currents supported firing with sparse input. Thus, A-type potassium currents
663 enhance synchrony-coding, whereas calcium and sodium currents favor rate-coding. These
664 currents modulate dendritic integration in cortical and hippocampal dendrites (Stuart et al. 2015).
665 Our findings align with experimental evidence showing that inactivating T-type calcium currents
666 extend synaptic potentials (Connelly et al. 2016; Gillessen and Alzheimer 1997; Liu and Shipley
667 2008; Prescott and De Koninck 2005; Urban et al. 1998), while inactivating A-type potassium
668 channels shorten them (Hoffman et al. 1997; Mathews et al. 2010). Notably, we are the first to
669 show that transient sodium currents have a lengthening effect.
670
671 Our results align with previous computational simulations. For instance, Remme et al. (2011)
672 found that EPSP amplitude and duration decrease due to low-voltage-activated potassium
673 currents and increase due to persistent sodium currents. Ceballos et al. (2017b) reported that
674 persistent sodium current amplifies and prolongs EPSPs in a voltage-dependent manner.
675 Hoffman et al. (1997) showed that A-type potassium current activation reduces EPSP amplitude
676 in CA1 pyramidal neuron dendrites. Branco et al. (2016) demonstrated that balanced persistent
677 sodium and potassium currents can generate long-lasting EPSPs, enabling near-perfect synaptic
678 integration. Additionally, Carter et al. (2012) used computational models to predict that sodium

currents mediate subthreshold transient current activation by EPSPs. The inactivating A-type potassium and T-type calcium currents have also been studied in simulations in the context of resonance (Rathour and Narayanan, 2012). However, to our knowledge, we are the first to investigate their role in dendritic spike integration modes under *in-vivo*-like conditions.

Future work should explore other factors influencing the activation/inactivation properties of ionic currents and systematize findings across species. For example, sodium and potassium current voltage-dependence is more depolarized in humans than mice (Wilbers 2023), and isoflurane hyperpolarizes sodium current inactivation (Qiu et al. 2023). Neuromodulation also enhances sodium current inactivation (Chen et al. 2006). Though we focus on *in vivo*-like states, future studies could investigate how alternating states affect synaptic integration.

Author contributions

C.C.C. and R.F.O.P. designed the research. C.C.C. carried out all simulations and analyzed the data. C.C.C. and R.F.O.P. wrote the article.

References

1. Remme, M. W., & Rinzel, J. (2011). Role of active dendritic conductances in subthreshold input integration. Journal of computational neuroscience, 31, 13-30.

2. Ceballos, C. C., Roque, A. C., & Leão, R. M. (2017a). The role of negative conductances in neuronal subthreshold properties and synaptic integration. Biophysical reviews, 9, 827-834.

3. Ceballos, C. C., Roque, A. C., & Leao, R. M. (2017b). A negative slope conductance of the persistent sodium current prolongs subthreshold depolarizations. Biophysical Journal, 113(10), 2207-2217.

4. Ceballos, C. C., Pena, R. F., Roque, A. C., & Leão, R. M. (2018). Non-Decaying postsynaptic potentials and delayed spikes in hippocampal pyramidal neurons generated by a zero slope conductance created by the persistent Na+ current. Channels, 12(1), 81-88.

5. Richardson, M. J., Brunel, N., & Hakim, V. (2003). From subthreshold to firing-rate resonance. Journal of neurophysiology, 89(5), 2538-2554.

6. Liu S, Shipley MT (2008) Intrinsic conductances actively shape excitatory and inhibitory postsynaptic responses in olfactory bulb external tufted cells. J Neurosci 28:10311–10322

7. Prescott SA, De Koninck Y (2005) Integration time in a subset of spinal lamina I neurons is lengthened by sodium and calcium currents acting synergistically to prolong subthreshold depolarization. J Neurosci 25:4743–4754

8. Hoffman DA, Magee JC, Colbert CM, Johnston D (1997) K+ channel regulation of signal propagation in dendrites of hippocampal pyramidal neurons. Nature 387:869–875

9. Mathews PJ, Jercog PE, Rinzel J, Scott LL, Golding NL (2010) Control of submillisecond synaptic timing in binaural coincidence detectors by Kv1 channels. Nat Neurosci 13:601–609

10. Farries MA, Kita H, Wilson CJ (2010) Dynamic spike threshold and zero membrane slope conductance shape the response of subthalamic neurons to cortical input. J Neurosci 30:13180–13191

11. Branco T, Tozer A, Magnus CJ, Sugino K, Tanaka S, Lee AK, Wood JN, Sternson SM (2016) Near-perfect synaptic integration by Na v 1.7 in hypothalamic neurons regulates body weight. Cell 165:1749–1761

12. Carter, B. C., Giessel, A. J., Sabatini, B. L., & Bean, B. P. (2012). Transient sodium current at subthreshold voltages: activation by EPSP waveforms. Neuron, 75(6), 1081-1093.

13. González-Burgos, G., & Barrionuevo, G. (2001). Voltage-gated sodium channels shape subthreshold EPSPs in layer 5 pyramidal neurons from rat prefrontal cortex. Journal of Neurophysiology, 86(4), 1671-1684.

14. Deleuze, C., David, F., Béhuret, S., Sadoc, G., Shin, H. S., Uebele, V. N., ... & Bal, T. (2012). T-type calcium channels consolidate tonic action potential output of thalamic neurons to neocortex. Journal of Neuroscience, 32(35), 12228-12236.

15. Rudolph, M., & Destexhe, A. (2003). Tuning neocortical pyramidal neurons between integrators and coincidence detectors. Journal of computational neuroscience, 14, 239-251.

16. Brette, R. (2015). Philosophy of the spike: rate-based vs. spike-based theories of the brain. Frontiers in systems neuroscience, 9, 140675.

17. Hong, S., Ratté, S., Prescott, S. A., & De Schutter, E. (2012). Single neuron firing properties impact correlation-based population coding. Journal of Neuroscience, 32(4), 1413-1428.

18. Azouz, R., & Gray, C. M. (2000). Dynamic spike threshold reveals a mechanism for synaptic coincidence detection in cortical neurons in vivo. Proceedings of the National Academy of Sciences, 97(14), 8110-8115.

19. Wilbers, R., Metodieva, V. D., Duverdin, S., Heyer, D. B., Galakhova, A. A., Mertens, E. J., ... & Goriounova, N. A. (2023). Human voltage-gated Na+ and K+ channel properties underlie sustained fast AP signaling. Science advances, 9(41), eade3300.

767

768 20. Qiu, J., Yang, Y., Liu, J., Zhao, W., Li, Q., Zhu, T., ... & Zhou, C. (2023). The volatile
769 anesthetic isoflurane differentially inhibits voltage-gated sodium channel currents
770 between pyramidal and parvalbumin neurons in the prefrontal cortex. Frontiers in Neural
771 Circuits, 17, 1185095.

772

773 21. Chen, Y., Frank, H. Y., Surmeier, D. J., Scheuer, T., & Catterall, W. A. (2006).
774 Neuromodulation of Na+ channel slow inactivation via cAMP-dependent protein kinase
775 and protein kinase C. Neuron, 49(3), 409-420.

776

777 22. Fukaya, R., Yamada, R., & Kuba, H. (2018). Tonotopic variation of the T-type Ca2+
778 current in avian auditory coincidence detector neurons. Journal of Neuroscience, 38(2),
779 335-346.

780

781 23. Waters, J., & Helmchen, F. (2006). Background synaptic activity is sparse in
782 neocortex. Journal of Neuroscience, 26(32), 8267-8277.

783

784 24. Bourdeau, M. L., Morin, F., Laurent, C. E., Azzi, M., & Lacaille, J. C. (2007). Kv4. 3-
785 mediated A-type K+ currents underlie rhythmic activity in hippocampal
786 interneurons. Journal of Neuroscience, 27(8), 1942-1953.

787

25. Rathour, R. K., Malik, R., & Narayanan, R. (2016). Transient potassium channels augment degeneracy in hippocampal active dendritic spectral tuning. Scientific reports, 6(1), 24678.

26. Adam, Y., Kim, J. J., Lou, S., Zhao, Y., Xie, M. E., Brinks, D., ... & Cohen, A. E. (2019). Voltage imaging and optogenetics reveal behaviour-dependent changes in hippocampal dynamics. Nature, 569(7756), 413-417.

27. Malezieux, M., Kees, A. L., & Mulle, C. (2020). Theta oscillations coincide with sustained hyperpolarization in CA3 pyramidal cells, underlying decreased firing. Cell Reports, 32(1).

28. Connelly, W. M., Crunelli, V., & Errington, A. C. (2016). Passive synaptic normalization and input synchrony-dependent amplification of cortical feedback in thalamocortical neuron dendrites. Journal of Neuroscience, 36(13), 3735-3754.

29. Gillessen, T., & Alzheimer, C. (1997). Amplification of EPSPs by low Ni2+-and amiloride-sensitive Ca2+ channels in apical dendrites of rat CA1 pyramidal neurons. Journal of neurophysiology, 77(3), 1639-1643.

30. Peng, H., Bian, X. L., Ma, F. C., & Wang, K. W. (2017). Pharmacological modulation of the voltage-gated neuronal Kv7/KCNQ/M-channel alters the intrinsic excitability and

synaptic responses of pyramidal neurons in rat prefrontal cortex slices. Acta Pharmacologica Sinica, 38(9), 1248-1256.

31. Urban, N. N., Henze, D. A., & Barrionuevo, G. (1998). Amplification of perforant-path EPSPs in CA3 pyramidal cells by LVA calcium and sodium channels. Journal of Neurophysiology, 80(3), 1558-1561.

32. Stuart, G., & Sakmann, B. (1995). Amplification of EPSPs by axosomatic sodium channels in neocortical pyramidal neurons. Neuron, 15(5), 1065-1076.

33. Andreasen, M., & Lambert, J. D. (1999). Somatic amplification of distally generated subthreshold EPSPs in rat hippocampal pyramidal neurones. The Journal of Physiology, 519(1), 85-100.

34. Evans, R. C., Zhu, M., & Khaliq, Z. M. (2017). Dopamine inhibition differentially controls excitability of substantia nigra dopamine neuron subpopulations through T-type calcium channels. Journal of Neuroscience, 37(13), 3704-3720.

35. Hönigsperger, C., Marosi, M., Murphy, R., & Storm, J. F. (2015). Dorsoventral differences in Kv7/M-current and its impact on resonance, temporal summation and excitability in rat hippocampal pyramidal cells. The Journal of physiology, 593(7), 1551-1580.

36. Hsu, C. L., Zhao, X., Milstein, A. D., & Spruston, N. (2018). Persistent sodium current mediates the steep voltage dependence of spatial coding in hippocampal pyramidal neurons. Neuron, 99(1), 147-162.

37. Hage, T. A., Sun, Y., & Khaliq, Z. M. (2016). Electrical and Ca2+ signaling in dendritic spines of substantia nigra dopaminergic neurons. Elife, 5, e13905.

38. Seong, H. J., Behnia, R., & Carter, A. G. (2014). Impact of subthreshold membrane potential on synaptic responses at dendritic spines of layer 5 pyramidal neurons in the prefrontal cortex. Journal of neurophysiology, 111(10), 1960-1972.

39. Grunditz, Å., Holbro, N., Tian, L., Zuo, Y., & Oertner, T. G. (2008). Spine neck plasticity controls postsynaptic calcium signals through electrical compartmentalization. Journal of Neuroscience, 28(50), 13457-13466.

40. Izhikevich, E. M. (2007). Dynamical systems in neuroscience. MIT press.

41. Prince, L. Y., Tran, M. M., Grey, D., Saad, L., Chasiotis, H., Kwag, J., ... & Richards, B. A. (2021). Neocortical inhibitory interneuron subtypes are differentially attuned to synchrony-and rate-coded information. Communications Biology, 4(1), 935.

42. Hille, B. (2001). Ion Channels of Excitable Membranes Third Edition.

43. Stuart, G. J., & Spruston, N. (2015). Dendritic integration: 60 years of progress. Nature neuroscience, 18(12), 1713-1721.

44. Engbers, J. D., Anderson, D., Asmara, H., Rehak, R., Mehaffey, W. H., Hameed, S., ... & Turner, R. W. (2012). Intermediate conductance calcium-activated potassium channels modulate summation of parallel fiber input in cerebellar Purkinje cells. Proceedings of the National Academy of Sciences, 109(7), 2601-2606.

45. Jaffe, D. B., Ross, W. N., Lisman, J. E., Lasser-Ross, N., Miyakawa, H., & Johnston, D. (1994). A model for dendritic Ca2+ accumulation in hippocampal pyramidal neurons based on fluorescence imaging measurements. Journal of Neurophysiology, 71(3), 1065-1077.

46. Korngreen, A., & Sakmann, B. (2000). Voltage-gated K+ channels in layer 5 neocortical pyramidal neurones from young rats: subtypes and gradients. The Journal of physiology, 525(3), 621-639.

47. Dougalis, A. G., Matthews, G. A., Liss, B., & Ungless, M. A. (2017). Ionic currents influencing spontaneous firing and pacemaker frequency in dopamine neurons of the ventrolateral periaqueductal gray and dorsal raphe nucleus (vlPAG/DRN): A voltage-clamp and computational modelling study. Journal of Computational Neuroscience, 42, 275-305.

48. Moore, J. J., Ravassard, P. M., Ho, D., Acharya, L., Kees, A. L., Vuong, C., & Mehta, M. R. (2017). Dynamics of cortical dendritic membrane potential and spikes in freely behaving rats. Science, 355(6331), eaaj1497.

49. Ujfalussy, B. B., Makara, J. K., Lengyel, M., & Branco, T. (2018). Global and multiplexed dendritic computations under in vivo-like conditions. Neuron, 100(3), 579-592.

50. Dembrow, N. C., & Spain, W. J. (2022). Input rate encoding and gain control in dendrites of neocortical pyramidal neurons. Cell reports, 38(7).

51. Liao, Z., Gonzalez, K. C., Li, D. M., Yang, C. M., Holder, D., McClain, N. E., ... & Negrean, A. (2024). Functional architecture of intracellular oscillations in hippocampal dendrites. Nature Communications, 15(1), 6295.

52. Roome, C. J., & Kuhn, B. (2020). Dendritic coincidence detection in Purkinje neurons of awake mice. elife, 9, e59619.

53. Ratté, S., Hong, S., De Schutter, E., & Prescott, S. A. (2013). Impact of neuronal properties on network coding: roles of spike initiation dynamics and robust synchrony transfer. Neuron, 78(5), 758-772.

54. Stoll, A., Maier, A., Krauss, P., Gerum, R., & Schilling, A. (2023). Coincidence detection and integration behavior in spiking neural networks. *Cognitive Neurodynamics*, 1-13.

55. Dembrow, N. C., Zemelman, B. V., & Johnston, D. (2015). Temporal dynamics of L5 dendrites in medial prefrontal cortex regulate integration versus coincidence detection of afferent inputs. *Journal of Neuroscience*, *35*(11), 4501-4514.

56. Harris, K. D., & Thiele, A. (2011). Cortical state and attention. *Nature reviews neuroscience*, *12*(9), 509-523.

57. Katz, Y., Menon, V., Nicholson, D. A., Geinisman, Y., Kath, W. L., & Spruston, N. (2009). Synapse distribution suggests a two-stage model of dendritic integration in CA1 pyramidal neurons. Neuron, 63(2), 171-177.

58. Polsky, A., Mel, B. W., & Schiller, J. (2004). Computational subunits in thin dendrites of pyramidal cells. Nature neuroscience, 7(6), 621-627.

59. Rathour, R. K., & Narayanan, R. (2012). Inactivating ion channels augment robustness of subthreshold intrinsic response dynamics to parametric variability in hippocampal model neurons. The Journal of physiology, 590(22), 5629-5652.